ACS OMEGA

Open Access

http://pubs.acs.org/journal/acsodf

Article

Influence of the Electron Transport Layer on the Performance of Perovskite Solar Cells under Low Illuminance Conditions

Tomoki Asada, Itaru Raifuku,* Fumihiro Murata, Kazuya Hayashi, Hiroaki Sugiyama, and Yasuaki Ishikawa*

Cite This: *ACS Omega* 2024, 9, 32893−32900

Read Online

ACCESS | Metrics & More | Article Recommendations | Supporting Information

ABSTRACT: Owing to the tunable band gap of metal-halide perovskite compounds, perovskite solar cells (PSCs) are promising energy-harvesting devices for indoor applications. Since the electron transport layer (ETL) plays a critical role in the performance of PSCs, selecting a suitable ETL is important for improving the performance of PSCs. Here, we compared the characteristics of PSCs employing TiO_2 and SnO_2, which are widely used as ETLs in PSCs, under low illuminance conditions. Electrochemical impedance spectroscopy revealed that PSCs employing SnO_2 as the ETL exhibited lower charge transfer resistance than those employing TiO_2 in low light intensity environments. Consequently, SnO_2-based PSCs showed a higher power conversion efficiency of 27.7% than that of TiO_2-based PSCs (22.5%) under 1000 lx white LED illumination. Space-charge-limited current measurements have shown that the defect density of ETLs strongly affects the performance of PSCs, especially under low illuminance conditions. We believe that this report provides an effective strategy for selecting appropriate ETLs for indoor applications of PSCs.

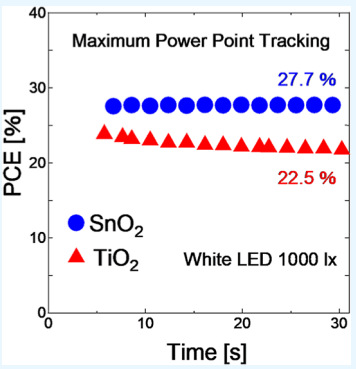

INTRODUCTION

Perovskite solar cells (PSCs) were first reported in 2009 by Miyasaka et al.,[1] where the power conversion efficiency (PCE) of PSCs was reported as 3.8%. Recently, a PCE of over 26% has been achieved by optimizing the composition of perovskites, developing charge transport materials, and defect management in the device.[2−10] In recent years, the development of PSC-based applications has received considerable attention. One of the applications is tandem solar cells, and tandem solar cells combined with silicon solar cells, CuInGa(Se,S) solar cells, and PSCs have been reported.[11,12] Si/PSC tandem solar cells have been actively investigated, and a PCE of 33.9% has been achieved.[13] Furthermore, PSCs can work more efficiently than other types of solar cells even in low light intensity environments such as indoor conditions. This is attributed to their device structure and the defect tolerance of perovskite compounds.[14−16] Combined with their lightweight and flexibility, PSCs are expected to be applied as power sources for internet of things devices.[17,18]

There have been several reports on improving the PCE of PSCs under low light intensity condition. Because the spectra of sun light and indoor lightings are quite different, changing the band gap of the light absorber is an effective way to improve the performance of solar cells under indoor lightings. For example, Raifuku et al. applied different perovskite compounds as the light absorber of PSCs and evaluated the performance under fluorescent lamp illumination. They controlled the band gap of perovskite compounds by changing the ratio of iodide and bromide in $Cs_{0.05}FA_{0.79}MA_{0.16}Pb(I_{1-x}Br_x)_3$, where FA and MA are formamidine and methylammonium, respectively. They recorded a PCE of 30.3% under 200 lx fluorescent lamp illumination with PSCs employing $Cs_{0.05}FA_{0.79}MA_{0.16}Pb(I_{0.50}Br_{0.50})_3$ which has a band gap of 1.8 eV.[19] Cheng et al. reported a PCE of 36.2% under 1000 lx fluorescent lamp illumination by employing triple-anion $MAPbI_{2-x}BrCl_x$.[20] They found that chloride doping suppresses the trap-states and nonradiative recombination losses. As another effective strategy, surface passivation of the perovskite layer has also been investigated. Li et al. applied phenethylammonium iodide (PEAI), phenethylammonium bromide (PEABr), and phenethylammonium chloride (PEACl) to reduce the surface defects of wide band gap perovskite $(FA_{0.6}MA_{0.4})_{0.9}Cs_{0.1}Pb(I_{0.6}Br_{0.4})_3$.[21] They found that PEACl effectively suppressed the halide segregation in perovskite films and prolonged the carrier lifetime of perovskite films. They reported a PCE of 35.6% under 1000 lx white LED illumination by employing PEACl-treated wide band gap perovskite. He et al. applied CH_3O-PEABr as a surface passivator for perovskite compounds. After optimizing the concentration of passivator and film thickness of each component in PSCs, they recorded a PCE of 40.1% under

Received: April 16, 2024
Revised: May 29, 2024
Accepted: July 11, 2024
Published: July 18, 2024

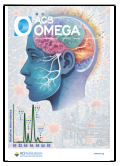

824.5 lx warm-white LED illumination.[22] Although the PCE of PSCs under indoor lightings exceeded 40%, there is still room to improve the PCE according to theoretical calculation.[23]

Some studies have reported that electron transport layer (ETL) has a significant impact on the performance of PSCs in low light intensity environments. In the case of PSCs using planar-TiO_2 and mesoporous-TiO_2 as ETLs, the planar-type can maintain a higher open-circuit voltage (V_{OC}) in low light intensity environments than the mesoporous-type. This is because the internal resistance of PSCs employing mesoporous TiO_2 is larger than that of PSCs employing planar TiO_2.[14] This report shows that the band gap and defect control of the perovskite layer, as well as the internal resistance of the device, which is varied by the ETL, play important roles in improving the performance of PSCs in low light environments. Therefore, the investigation and selection of an ETL that can suppress the increase in the internal resistance of the device under low light conditions is considered one of the key issues for the indoor application of PSCs.

Among the various n-type semiconductors, TiO_2 and SnO_2 are widely used as ETLs in PSCs. Recently, SnO_2 has attracted attention as a suitable ETL due to its deeper conduction band and higher conductivity than TiO_2, and its superiority in terms of low-temperature deposition.[24] In fact, SnO_2-based PSCs have shown high PCE under the air mass 1.5 global (AM1.5G) spectrum.[8,9] However, comparisons of the performance of SnO_2-based PSCs and TiO_2-based PSCs under low illuminance conditions have yet to be conducted.

TiO_2 and SnO_2 behave as n-type semiconductors due to oxygen vacancies and interstitial metal atoms that act as donors.[25,26] The formed donor levels are ionized and cause impurity scattering during electron transport in the ETL. Therefore, regardless of the material used as the ETL, the amount of defects in the ETL is considered an important parameter affecting the charge transport properties.

In this study, the characteristics of planar-type PSCs employing SnO_2 and TiO_2 as ETLs were evaluated under 1 sun condition (AM1.5G, 100 mW/cm^2) and low illuminance conditions, focusing on the carrier transport mechanisms such as impurity scattering in the ETL. We found that PSCs employing SnO_2 exhibited a higher PCE under 0.01 sun and 1000 lx white LED illumination. Impedance spectroscopy revealed that PSCs employing SnO_2 showed lower charge transfer resistance than TiO_2-based PSCs under low illuminance conditions. These results indicate that material selection and the charge transport mechanism of the charge transport layer should be considered to improve the performance of PSCs under low illuminance conditions.

EXPERIMENTAL SECTION

Materials. Transparent conductive oxide (TCO)-coated glass substrates (GEOMATEC Co., Ltd. 1052, 10 Ω sq^{-1}), SnO_2 colloid dispersion (15 wt % in H_2O, Alfa Aesar), titanium diisopropoxide bis (acetylacetonate) [Ti(ac), 75 wt % in isopropanol, Aldrich], *N*,*N*-dimethylformamide (DMF, Aldrich), dimethyl sulfoxide (DMSO, Aldrich), chlorobenzene (CBZ, Aldrich), 2-phenylethylamine hydrochloride (PEACl, Aldrich), lithium bis(trifluoromethanesulfonyl)imide (LiTFSI, Aldrich), 4-*tert*-butylpyridine(Aldrich), lead iodide (PbI_2, TCI), lead bromide ($PbBr_2$, TCI), cesium iodide (CsI, TCI), formamidine iodide (FAI, TCI), methylamine bromide (MABr, TCI), hydrochloric acid (HCl, TCI), 1-butanol (TCI), 2,2′,7,7′-tetrakis(*N*,*N*-di-4-methoxyphenylamino)-9,9′-spirobifluorene (spiro-MeOTAD, Fujifilm Wako Chemicals), zinc powder (Fujifilm Wako Chemicals), 2-propanol (IPA, Fujifilm Wako Chemicals), acetonitrile (Fujifilm Wako Chemicals), and gold wire (Nilaco) were purchased and used without purification.

Device Fabrication. We fabricated PSCs with a device structure of TCO/ETL/$FA_{0.81}MA_{0.1}Cs_{0.09}Pb(I_{0.9}Br_{0.1})_3$/PEACl/spiro-OMeTAD/Au as follows. TCO-coated glass substrates (25 × 25 mm) were etched with zinc powder and 2 M HCl and sequentially cleaned via sonication with Semico clean 56 (Furuuchi Chemical Co.) for 10 min. This was followed by cleaning with deionized water, acetone, and ethanol for 5, 10, and 5 min, respectively. The substrates were then cleaned for 30 min using a UV−ozone cleaner. Thereafter, 20 nm thick TiO_2 or SnO_2 films were deposited on the TCO substrates as the ETL. The thickness of the ETL was measured using a profilometer. TiO_2 films were deposited on TCO substrates by spin-coating 0.14 M Ti(ac) 1-butanol solution at 2000 rpm for 40 s, followed by annealing at 450 °C for 30 min. Whereas SnO_2 films were deposited on TCO substrates by spin-coating SnO_2 colloid dispersion diluted in deionized water (1:2 volume ratio) at 4000 rpm for 30 s, followed by annealing at 150 °C for 30 min. After forming the ETL, the substrate was treated with a UV−ozone cleaner for 30 min before depositing the perovskite layer. To form perovskite layer, 1.3 M $FA_{0.81}MA_{0.1}Cs_{0.09}Pb(I_{0.9}Br_{0.1})_3$ solution in 7:3 volume ratio of DMF/DMSO solvent was spin-coated on the ETL at 5000 rpm for 27.5 s, followed by annealing at 100 °C for 60 min. During the spin coating process, 160 μL of CBZ was dropped onto the rotating substrate 13 s before the end of the spin coating process. Thereafter, 0.75 mg/mL PEACl solution dissolved in IPA was spin-coated at 4000 rpm for 20 s, followed by annealing at 80 °C for 30 min to passivate the surface of perovskite layer. To form a hole transport layer, a spiro-OMeTAD solution dissolved in CBZ was spin-coated onto the PEACl layer at 4000 rpm for 26 s. Finally, 60 nm gold electrodes were formed by thermal evaporation.

Characterization. The current density−voltage (J−V) characteristics of the PSCs were measured under AM1.5G illumination using a solar simulator (high-pressure xenon lamp class AAA solar simulator, Yamashita Denso Co.). To control the light intensity, we inserted ND filters (ND10T-50S, ND01T-50S, Shibuya Optical Co., Ltd.) between the PSCs and light source. To evaluate the performance of the PSCs under indoor lighting, we used a 1000 lx (0.3002 mW/cm^2) white LED (BLD-100, Bunkoukeiki Co., Ltd.) as the light source. The scan speed was set to 69 mV/s. Maximum power point tracking (MPPT) measurements were performed using a VK PA 100 (SPD Laboratory, Inc.) under AM1.5G or white LED illumination. The active area of the samples was set to 0.152 cm^2. We performed electrochemical impedance spectroscopy (EIS) on the PSCs in the frequency range of 100 mHz−1 MHz using an electrochemical workstation (SP-150, Bio-Logic). An AC voltage with a perturbation amplitude of 100 mV was applied during EIS measurements. Scanning electron microscopy (SEM) images of the perovskite films were obtained using a field emission scanning electron microscope (Carl Zeiss AG, ULTRA55). The X-ray diffraction (XRD) patterns of the TiO_2, SnO_2, and perovskite films were measured using an X'PERT-PRO MRD (Spectris). Atomic force microscopy (AFM) images of TiO_2 and SnO_2 films were obtained using SPM-9700 (SHIMADZU). The absorption spectra of the perovskite films were recorded with an

https://doi.org/10.1021/acsomega.4c03643
ACS Omega 2024, 9, 32893−32900

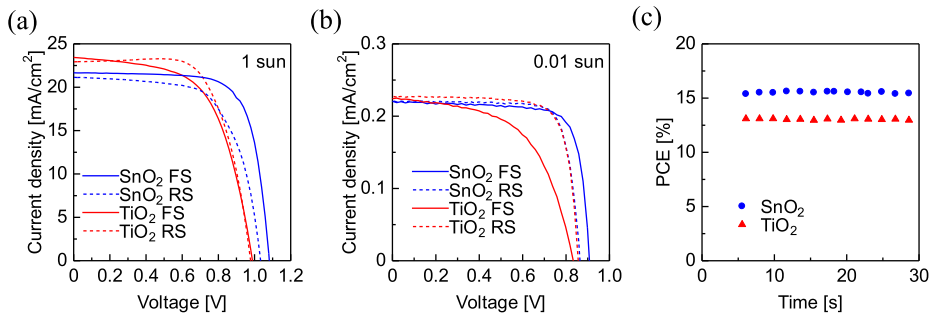

Figure 1. $J-V$ curves of PSCs employing SnO_2 (blue) and TiO_2 (red) as ETLs measured under (a) 1 sun and (b) 0.01 sun illumination. The solid and dashed lines represent the $J-V$ curves obtained in FS and RS, respectively. (c) PCE estimated from MPPT measurements under 0.01 sun illumination.

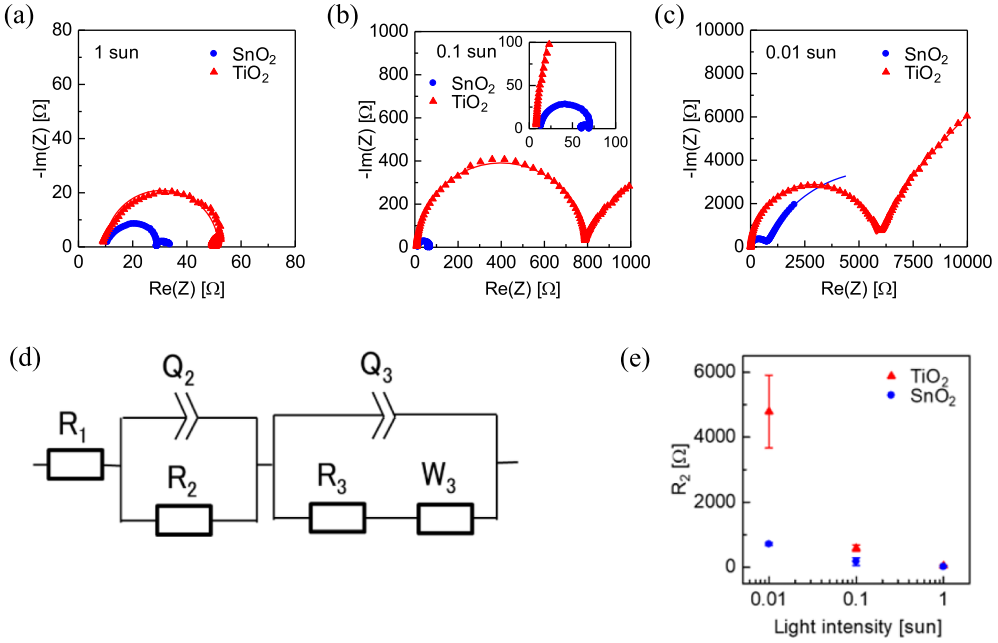

Figure 2. Nyquist plots of PSCs employing different ETLs measured under (a) 1 sun, (b) 0.1 sun (inset: enlarged view of the area near the origin), and (c) 0.01 sun illumination. (d) Equivalent circuit used to fit the Nyquist plots. (e) Light intensity dependence of charge transfer resistance (R_2) of PSCs employing different ETLs. The average values were calculated from five samples.

ultraviolet/visible light/near-infrared spectrophotometer (JASCO, V-770).

RESULTS AND DISCUSSION

Figure 1a shows the $J-V$ curves of the best-performing PSCs employing TiO_2 or SnO_2 as the ETLs measured under 1 sun condition. The solid and dashed lines represent $J-V$ curves obtained from forward scan (FS, from −0.2 to 1.2 V) and reverse scan (RS, from 1.2 to −0.2 V), respectively. The $J-V$ characteristics of the PSCs are summarized in Table S1. In FS, PSCs employing TiO_2 and SnO_2 showed PCEs of 13.9 and 17.1%, respectively. In contrast, in RS, PSCs employing TiO_2 and SnO_2 showed PCEs of 15.1 and 14.2%, respectively. TiO_2-based PSCs showed a higher PCE with a higher fill factor (FF) when the samples were analyzed in the RS. This phenomenon is a well-known hysteresis behavior that originates from the capacitor and accumulating carriers formed at the ETL/perovskite interface.[27] However, PSCs with SnO_2 behaved differently; the PCE obtained from the RS was lower than that of the FS. This phenomenon is referred to as inverted hysteresis and has rarely been reported compared with normal hysteresis. To the best of our knowledge, Tress et al. were the first to report this phenomenon in 2016.[28] In their study, it was found that the addition of Al_2O_3 to mesoporous TiO_2 altered the interface between the ETL and the perovskite, resulting in inverted hysteresis. They have also reported that the magnitude of inverted hysteresis varies depending on the scan rate during $J-V$ measurements, and PSCs that show inverted hysteresis exhibited negative capacitance in Nyquist plots when the EIS measurements were conducted with bias voltage.[29] Figure S1 shows the $J-V$ curves of PSCs employing SnO_2 measured at different scan rates obtained in our research. The inverted hysteresis became larger when the $J-V$ curves were measured at a lower scan rate. A hysteresis index (HI), which is one of the indicators of the degree of hysteresis, is defined as $(PCE_{reverse} - PCE_{forward})/PCE_{reverse}$, where $PCE_{reverse}$ and $PCE_{forward}$ correspond to PCE calculated from $J-V$ curves measured under reverse and FS, respectively.[30] The absolute values of HI increased from 0.03 to 0.41 by varying scan rate of $J-V$ measurements. It is reported that the inverted hysteresis appears when the halide vacancy accumulates at the ETL/perovskite interface and interacts with ETL.[31] We assume that

https://doi.org/10.1021/acsomega.4c03643
ACS Omega 2024, 9, 32893−32900

there is enough time for the halide vacancy to accumulate at the ETL/perovskite interface and interact with the ETL, resulting in a larger inverted hysteresis at a lower scan rate. Figure S2 shows the Nyquist plot of a PSC employing SnO_2 measured at a bias voltage of 0.9 V. A certain behavior associated with negative capacitance was observed in the low-frequency range of the Nyquist plot, as shown in Figure S2. These results were consistent with those of a previous report.[29] When comparing the average values of the five PCE, the SnO_2-based PSCs showed slightly higher PCE in both forward and reverse scans, as shown in Table S2.

We compared the characteristics of both PSCs under low illuminance conditions. Figure 1b shows the $J-V$ curves of PSCs employing TiO_2 or SnO_2 as ETLs measured under 0.01 sun condition. The $J-V$ characteristics of the best-performing PSCs are summarized in Table S3. Although the short-circuit current density (J_{SC}) and V_{OC} of both PSCs decreased with decreasing light intensity, the behavior of the FF was different. The FF calculated from $J-V$ curves measured in the RS increased under the 0.01 sun condition, regardless of the ETLs. Consequently, both PSCs showed similar PCE under 0.01 sun condition. In contrast, in the case of the FS, TiO_2-based PSCs showed a rapid decrease in the FF under 0.01 sun condition. This complex behavior makes it difficult to compare the performances of both PSCs from $J-V$ measurements. Therefore, MPPT measurements were performed to compare the performance of both PSCs while eliminating the effects of hysteresis. Figure 1c shows the PCE of PSCs employing TiO_2 or SnO_2 as ETLs, as estimated from the MPPT measurements. After 30 s MPPT measurements, PSCs employing TiO_2 and SnO_2 showed PCEs of 13.0 and 15.5%, respectively. From the MPPT measurements, it was confirmed that the PSCs employing SnO_2 exhibited a higher PCE than those employing TiO_2 under 0.01 sun illumination. The PCE of PSCs calculated from $J-V$ curves and MPPT measurements are summarized in Table S4.

Figure S3 shows the light intensity dependence of the V_{OC} values of both TiO_2 and SnO_2-based PSCs. As shown in Figure S3, TiO_2-based PSCs showed lower ideality factor (1.30) than the SnO_2-based one (1.45), and the latter one even showed better performances under 0.01 sun condition. This result indicates that fewer interface recombination occurs at the TiO_2/perovskite interface than the SnO_2/perovskite interface.

To evaluate the internal resistance of PSCs employing TiO_2 or SnO_2 as their ETLs, EIS measurements were performed under different light intensities. During EIS measurements, a bias direct current (DC) can be applied to the samples. However, when EIS measurement is performed under the V_{OC} condition, diffusion and drift currents become negligible and few photogenerated carriers are injected into the ETL.[32] To evaluate the influence of ETLs, we have performed EIS measurements at DC 0 V (without DC bias voltage). Figure 2a–c shows the Nyquist plots of the PSCs measured under 1, 0.1, and 0.01 sun illumination. The dots and lines represent the values obtained from EIS and fitted curves using an equivalent circuit (Figure 2d), respectively. In the equivalent circuit, R_1 [cross point with Re(Z) axis] was associated with the series resistance of the device. R_2 (first semicircle) and R_3 (second semicircle) were associated with the charge transfer resistance and charge recombination resistance, respectively.[33−35] W_3 was associated with Warburg resistance. Although Q_2 and Q_3 are considered as interfacial capacitance originated from charge accumulation at HTL/perovskite or ETL/perovskite interfaces, physical meaning in actual device needs to be investigated more. Here, we focused on the difference in charge transfer resistance (R_2) to compare the characteristics of TiO_2 and SnO_2. PSCs employing SnO_2 exhibited smaller semicircles than the TiO_2-based one regardless of the light intensity. This indicated that SnO_2-based PSCs had a smaller charge transfer resistance than TiO_2-based PSCs. Figure 2e shows the light-intensity dependence of the average charge transfer resistance of the five samples, as estimated by equivalent circuit analysis. Under 1 sun condition, PSCs employing TiO_2 and SnO_2 as ETLs exhibited charge transfer resistances of 46.0 and 15.1 Ω, respectively. When the light intensity was decreased to 0.01 sun, the charge transfer resistance of TiO_2-based PSCs increased to 4790 Ω. In contrast, SnO_2-based PSCs showed a charge transfer resistance of 713 Ω under the same conditions. We presume that the lower charge transfer resistance of SnO_2-based PSCs is the origin of the better low illuminance performance of SnO_2-based PSCs, although SnO_2-based PSCs showed higher ideality factor than TiO_2-based PSCs. The average charge transfer resistances of the five samples under various light intensities are summarized in Table 1.

Table 1. Average Charge Transfer Resistance (R_2) of PSCs Employing TiO_2 or SnO_2 as the ETLs[a]

light intensity [sun]	0.01	0.1	1
$R_2(SnO_2)$ [Ω]	713 ± 65	175 ± 87	15.1 ± 2.9
$R_2(TiO_2)$ [Ω]	4790 ± 810	588 ± 114	46.0 ± 11.2

[a]The values were calculated from five samples.

Figure S4 shows AFM images of TiO_2 and SnO_2 films. Crystal grains are clearly observed in AFM image of TiO_2, whereas there were only localized crystal grains in AFM image of SnO_2. The arithmetic mean roughness (R_a) and root-mean-square roughness (R_q) of both films are summarized in Table S5. As shown in Table S5, both films showed similar surface roughness. Therefore, we assume that the difference in the morphology of ETLs might not affect the performance of PSCs under low illuminance conditions.

Figure S5 shows SEM images of the perovskite films deposited on the TiO_2 and SnO_2 films. No significant changes in the crystal grain size of the perovskite or surface morphology were observed when the perovskite films were deposited on different ETLs. Figure S6 shows the XRD patterns of the perovskite films deposited on TiO_2 and SnO_2 films. As no peaks related to the ETLs were observed, the diffraction patterns must have originated from the perovskite films. Because there were no significant changes in the peak position and peak intensity, it was considered that the crystallinity of the perovskite films is not significantly affected by the ETLs. Therefore, the changes in the charge transfer resistance in PCSs employing TiO_2 or SnO_2 films were considered to originate mainly from the difference in ETLs.

To clarify whether R_2 in Nyquist plots is related to the charge transfer resistance in ETL, EIS measurements were performed using PSCs employing 20, 60, and 100 nm thick SnO_2. The thickness of the ETL was measured using a profilometer. Figure 3a–c shows the Nyquist plots of PSCs measured under 1, 0.1, and 0.01 sun illumination, respectively. The dots and lines represent the measured values and fitted curves using an equivalent circuit (Figure 2d), respectively. The R_2 values obtained from the Nyquist plots are summarized

https://doi.org/10.1021/acsomega.4c03643
ACS Omega 2024, 9, 32893−32900

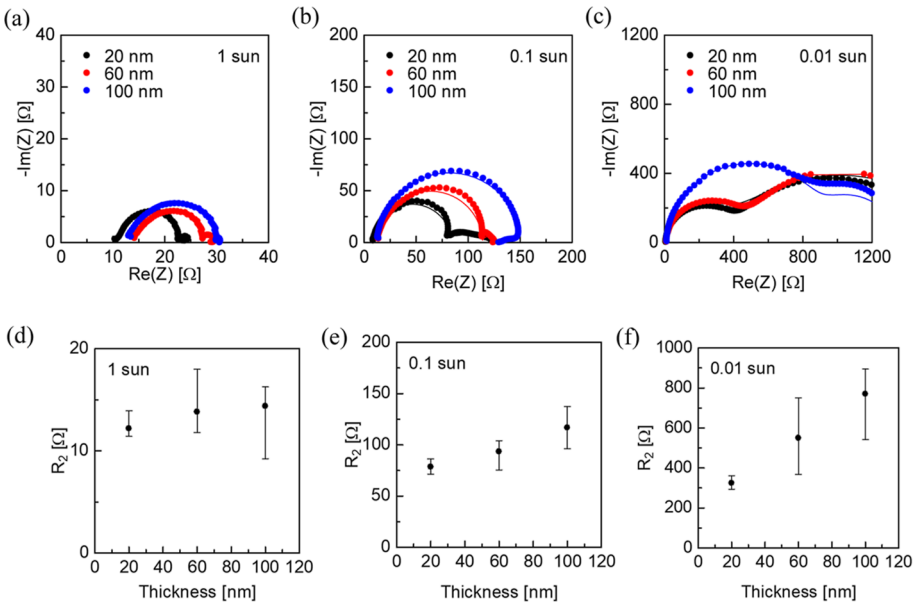

Figure 3. Nyquist plots of PSCs employing 20, 60, and 100 nm thick SnO_2 as ETL measured under (a) 1sun, (b) 0.1 sun, and (c) 0.01 sun illumination. Thickness dependence of R_2 values of PSCs under (d) 1 sun, (e) 0.1 sun, and (f) 0.01 sun illumination. The average values were calculated from four samples.

in Figure 3d–f and Table 2. The R_2 value increased as the thickness of SnO_2 increased, and the trend became more

Table 2. Average Charge Transfer Resistance (R_2) of PSCs Employing 20, 60, and 100 nm Thick SnO_2 as the ETL[a]

light intensity [sun]	0.01	0.1	1
20 nm SnO_2 [Ω]	324 ± 28.0	78.5 ± 6.3	12.2 ± 1.2
60 nm SnO_2 [Ω]	550 ± 160	93.5 ± 12.7	13.8 ± 2.8
100 nm SnO_2 [Ω]	770 ± 163	117 ± 17	14.4 ± 3.4

[a]The values were calculated from four samples.

obvious under low illuminance conditions. This result indicates that R_2 in the Nyquist plots contains information on the charge transfer resistance in ETLs.

We assume that the effects of defects become obvious under low illuminance conditions because the number of photogenerated carriers is lower than that of under 1 sun conditions. The space-charge-limited current (SCLC) measurements were performed on ETL sandwiched with electrodes (TCO/ETL/Au) to evaluate the defect density of ETLs. Figure 4a,b shows the I–V curves of the ETL devices. The I–V curves are divided into three different regions, ohmic region, trap filling region, and Child's region. The voltage at which the behavior changes from ohmic to trap filling is called the trap-filled limit voltage (V_{TFL}). The relationship between V_{TFL} and trap density (N_t) can be described as follows

$$N_t = \frac{2\varepsilon_0\varepsilon_r}{eL^2}V_{TFL}$$

where ε_0 is permittivity of vacuum, ε_r is the relative dielectric constant of ETL (SnO_2:12.5, TiO_2:40), e is the electron charge, and L is the thickness of ETLs (20 nm).[36−38] SnO_2 showed a trap density of 3.32×10^{18} cm^{-3}, which is lower than that of the TiO_2 (2.04×10^{19} cm^{-3}), as shown in Figure 4a,b. These trap sites are thought to originate from oxygen vacancies and interstitial metal (Sn and Ti) atoms that act as donor states for ETL.[25,26] Therefore, it is considered that electrons in TiO_2 are more strongly affected by impurity scattering than those in SnO_2 (Figure 4c), resulting in a higher charge transfer resistance. These results suggest that the difference in trap density between TiO_2 and SnO_2 is one of the reasons why PSCs with SnO_2 showed better performance under low illuminance conditions.

The carrier mobility of ETL was estimated using the SCLC model and the Mott Gurney law

$$J = \frac{9\varepsilon_0\varepsilon_r\mu V^2}{8L^3}$$

where J is the current density, ε_0 is the permittivity of vacuum, ε_r is the relative dielectric constant of ETL, μ is the carrier mobility, V is the applied voltage, and L is the thickness of ETLs (20 nm).[36] By fitting the slope of the Child's region in the J–V^2 curves (Figure S7), the carrier mobility of SnO_2 and TiO_2 were estimated to be 2.06×10^{-7} and 7.57×10^{-8} cm^2 V^{-1} s^{-1}, respectively. Figure 4d shows the XRD patterns of the TiO_2 and SnO_2 films deposited on the glass substrates. TiO_2 exhibits sharp peaks originating from the anatase structure, indicating that TiO_2 was highly crystallized during the fabrication process. In contrast, SnO_2 showed broad peaks, indicating that the SnO_2 films were composed of nanocrystals in amorphous tissue. These results indicate that SnO_2 has a higher electron mobility than TiO_2, even though SnO_2 films were mainly composed of the nanocrystalline phase. We assume that the origin of this phenomenon is the difference in orbitals that contribute to the electron transport in ETLs. In TiO_2, the generated electrons are transported via its 3d orbitals.[39] When the atoms are regularly arranged, the overlapping 3d orbitals facilitate carrier transport. However, when the atoms are not regularly arranged, the complex shapes of the 3d orbitals are less likely to overlap, rendering carrier transport more difficult (Figure 4e). In contrast, in the case of SnO_2, the generated electrons are transported via 5s orbitals.[39] Even if the atoms are not regularly arranged, the orbital overlap of SnO_2 is larger than that of TiO_2 due to its large principal quantum number and spherical orbital, facilitating carrier

https://doi.org/10.1021/acsomega.4c03643
ACS Omega 2024, 9, 32893−32900

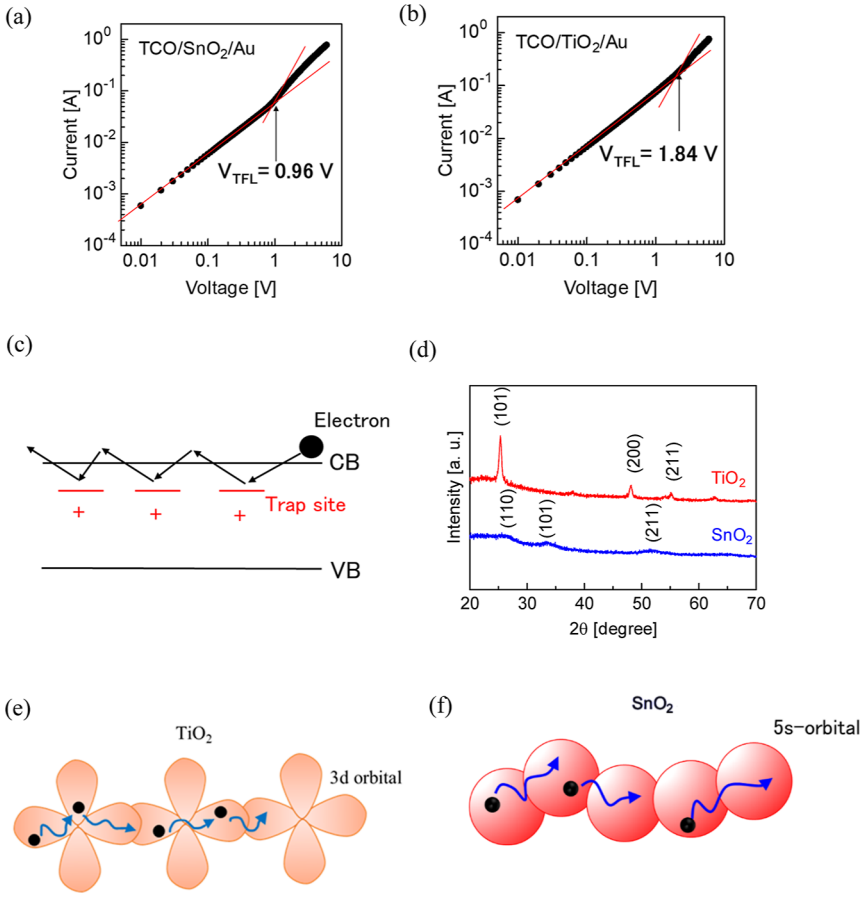

Figure 4. Current−voltage (I−V) curves obtained from SCLC measurements for (a) TCO/SnO_2/Au and (b) TCO/TiO_2/Au. (c) Schematic diagram of the trapping/detrapping process caused by impurity scattering. (d) XRD patterns of TiO_2 and SnO_2 films deposited on glass substrates. Schematic of electron transport mechanisms in (e) TiO_2 and (f) SnO_2.

transport (Figure 4f).[40,41] Furthermore, the strong polaron effect and high dielectric constant of TiO_2 are also considered to be the factor of the low electron mobility of TiO_2. It is reported that TiO_2 has a strongly localized Ti-3d state, which dominate the conduction band, with a flat conduction band edge energy dispersion.[42] This means that TiO_2 has a larger effective mass of conduction band electrons than SnO_2, resulting in lower electron mobility. These results imply that we need to focus not only on trap density but also on the orbitals that contribute to carrier transport to select optimal ETLs for indoor applications. Also, it is considered that the effect of the carrier transport orbitals of ETLs in PSCs should be studied in detail by comparing TiO_2 and SnO_2 at similar trap densities, but currently, it is a future challenge since controlling the trap density at similar ranges for both materials contains a technological difficulty in a printing process.

Finally, the J−V characteristics of the PSCs employing different ETLs were compared under white LED (1000 lx, 0.3002 mW/cm^2) illumination. The spectrum of the white LED light source used in this experiment is shown in Figure S8. Figure 5a shows the J−V curves of the PSCs measured under white LED illumination. The J−V characteristics of the best-performing PSCs are summarized in Table S6. Figure S9 shows the absorption spectra of the perovskite film used in this work. The perovskite does not absorb light above 800 nm. Compared to AM1.5G, which consists of a wide range of wavelengths from UV to IR, white LED contains limited wavelength of below 800 nm, as shown in Figure S8.

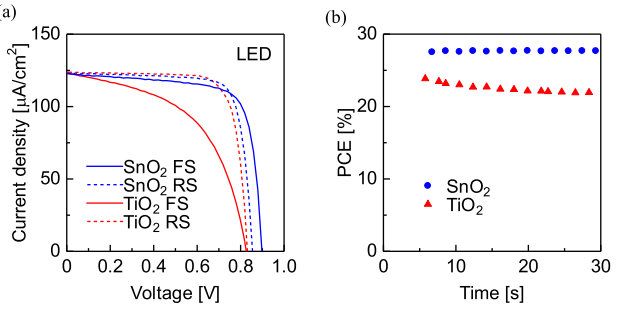

Figure 5. (a) J−V curves of the PSCs employing SnO_2 (blue) and TiO_2 (red) under 1000 lx white LED (0.3002 mW/cm^2) illumination. The solid and dashed lines represent J−V curves obtained from FS and RS, respectively. (b) PCE of PSCs obtained from MPPT measurements under 1000 lx white LED illumination.

Therefore, the PCE of PSCs under LED illumination showed a higher value compared to the PCE of PSCs under AM1.5G illumination. Although both the PSCs exhibited similar J_{SC} values, PSCs employing SnO_2-based PSCs showed slightly higher V_{OC} and FF values than that of TiO_2-based PSCs in both forward and RSs. PSCs employing TiO_2 as the ETL exhibited a larger hysteresis in J−V curves curve than SnO_2-based PSCs as similar to the case with 0.01 sun illumination. MPPT measurements were performed to compare the PCE of the two PSCs while eliminating the effects of hysteresis. Figure 5b shows the PCE of the PSCs calculated from the MPPT

https://doi.org/10.1021/acsomega.4c03643
ACS Omega 2024, 9, 32893−32900

measurements under white LED illumination. After 30 s MPPT measurements, PSCs employing SnO_2 and TiO_2 as their ETLs showed PCEs of 27.7 and 22.5%, respectively. It was confirmed that PSCs employing SnO_2 exhibited a higher PCE than that of TiO_2-based PSCs even under white LED illumination. SnO_2-based PSCs showed higher PCE than TiO_2 based PSCs even at an average value calculated from five samples as summarized in Table S7, indicating that SnO_2 is more suitable for ETL than TiO_2 even under an indoor light source.

CONCLUSIONS

In this study, the characteristics of PSCs employing TiO_2 and SnO_2 films as ETLs in low light intensity environments were compared. The SnO_2-based PSCs showed slightly higher PCE than TiO_2-based PSCs under 1 sun illumination. In contrast, the difference in PCE between SnO_2-based PSCs and TiO_2-based PSCs became larger under low illuminance conditions. This difference originated from the difference in the charge transfer resistance of each PSCs. EIS measurements and equivalent circuit analysis revealed that the charge transfer resistance of PSCs employing TiO_2 as the ETL increased under low light intensity. In contrast, PSCs employing SnO_2 as the ETL showed a lower charge transfer resistance than TiO_2-based PSCs under low illuminance conditions. SCLC measurements revealed that SnO_2 films have lower defect density than TiO_2 films. We presume that the different defect density is one of the origins of the lower charge transfer resistance of SnO_2 films since the defects cause impurity scattering and influence on the electron transport in ETLs. SCLC and XRD measurements revealed that SnO_2 films show higher carrier mobility than TiO_2 films, although TiO_2 films show higher crystallinity. We assume that this phenomenon is originated from the difference in the orbitals that contribute to carrier transport in ETLs. Furthermore, PSCs employing SnO_2 showed higher PCE of 27.7% than that of TiO_2-based one (22.5%) even under 1000 lx white LED illumination. Our results indicate that ETLs should be selected not only by focusing on conventional indicators such as band gap and energy levels but also by focusing on the charge transport mechanisms of materials to establish high-performance PSCs under low illuminance conditions.

ASSOCIATED CONTENT

Supporting Information

The Supporting Information is available free of charge at https://pubs.acs.org/doi/10.1021/acsomega.4c03643.

J−*V* curves and Nyquist plot of SnO_2-based PSCs showing inverted hysteresis, light intensity dependence of the V_{OC} of PSCs, AFM images of SnO_2 and TiO_2 films deposited on TCO substrates, SEM images and XRD patterns of perovskite films deposited on different ETLs, emission spectrum of the white LED light source, and detailed *J*−*V* characteristics of PSCs (PDF)

AUTHOR INFORMATION

Corresponding Authors

Itaru Raifuku − *Aoyama Gakuin University, Sagamihara-shi, Kanagawa 252-5258, Japan;* orcid.org/0000-0003-0351-2119; Phone: +81-42-759-6389; Email: ra-itaru@ee.aoyama.ac.jp

Yasuaki Ishikawa − *Aoyama Gakuin University, Sagamihara-shi, Kanagawa 252-5258, Japan;* orcid.org/0000-0003-4613-6117; Phone: +81-42-759-6255; Email: yishikawa@ee.aoyama.ac.jp

Authors

Tomoki Asada − *Aoyama Gakuin University, Sagamihara-shi, Kanagawa 252-5258, Japan*

Fumihiro Murata − *Aoyama Gakuin University, Sagamihara-shi, Kanagawa 252-5258, Japan*

Kazuya Hayashi − *Aoyama Gakuin University, Sagamihara-shi, Kanagawa 252-5258, Japan*

Hiroaki Sugiyama − *Aoyama Gakuin University, Sagamihara-shi, Kanagawa 252-5258, Japan*

Complete contact information is available at: https://pubs.acs.org/10.1021/acsomega.4c03643

Funding

There is nothing to declare.

Notes

The authors declare no competing financial interest.

ACKNOWLEDGMENTS

The authors acknowledge the Instrumental Analysis Center of Aoyama Gakuin University for XRD and SEM analyses.

REFERENCES

(1) Kojima, A.; Teshima, K.; Shirai, Y.; Miyasaka, T. Organometal Halide Perovskites as Visible-Light Sensitizers for Photovoltaic Cells. *J. Am. Chem. Soc.* **2009**, *131* (17), 6050−6051.

(2) Jung, H. S.; Park, N.-G. Perovskite Solar Cells: From Materials to Devices. *Small* **2015**, *11* (1), 10−25.

(3) Min, H.; Kim, M.; Lee, S.-U.; Kim, H.; Kim, G.; Choi, K.; Lee, J. H.; Seok, S. I. Efficient, stable solar cells by using inherent bandgap of α-phase formamidinium lead iodide. *Science* **2019**, *366* (6466), 749−753.

(4) Lee, M. M.; Teuscher, J.; Miyasaka, T.; Murakami, T. N.; Snaith, H. J. Efficient Hybrid Solar Cells Based on Meso-Superstructured Organometal Halide Perovskites. *Science* **2012**, *338* (6107), 643−647.

(5) Chen, J.; Dong, H.; Li, J.; Zhu, X.; Xu, J.; Pan, F.; Xu, R.; Xi, J.; Jiao, B.; Hou, X.; Wei Ng, K.; Wang, S.-P.; Wu, Z. Solar Cell Efficiency Exceeding 25% through Rb-Based Perovskitoid Scaffold Stabilizing the Buried Perovskite Surface. *ACS Energy Lett.* **2022**, *7* (10), 3685−3694.

(6) Kim, H.-S.; Lee, C.-R.; Im, J.-H.; Lee, K.-B.; Moehl, T.; Marchioro, A.; Moon, S.-J.; Humphry-Baker, R.; Yum, J.-H.; Moser, J. E.; Grätzel, M.; Park, N.-G. Lead Iodide Perovskite Sensitized All-Solid-State Submicron Thin Film Mesoscopic Solar Cell with Efficiency Exceeding 9%. *Sci. Rep.* **2012**, *2* (1), 591.

(7) Chen, J.; Yang, Y.; Dong, H.; Li, J.; Zhu, X.; Xu, J.; Pan, F.; Yuan, F.; Dai, J.; Jiao, B.; Hou, X.; Jen, A. K. Y.; Wu, Z. Highly efficient and stable perovskite solar cells enabled by low-dimensional perovskitoids. *Sci. Adv.* **2022**, *8* (4), No. eabk2722.

(8) Park, J.; Kim, J.; Yun, H.-S.; Paik, M. J.; Noh, E.; Mun, H. J.; Kim, M. G.; Shin, T. J.; Seok, S. I. Controlled growth of perovskite layers with volatile alkylammonium chlorides. *Nature* **2023**, *616* (7958), 724−730.

(9) Zhao, Y.; Ma, F.; Qu, Z.; Yu, S.; Shen, T.; Deng, H.-X.; Chu, X.; Peng, X.; Yuan, Y.; Zhang, X.; You, J. Inactive $(PbI_2)_2RbCl$ stabilizes perovskite films for efficient solar cells. *Science* **2022**, *377* (6605), 531−534.

(10) Zhang, X.; Qiu, W.; Song, W.; Hawash, Z.; Wang, Y.; Pradhan, B.; Zhang, Y.; Naumenko, D.; Amenitsch, H.; Moons, E.; Merckx, T.; Aguirre, A.; Abdulraheem, Y.; Aernouts, T.; Zhan, Y.; Kuang, Y.; Hofkens, J.; Poortmans, J. An Integrated Bulk and Surface

Modification Strategy for Gas-Quenched Inverted Perovskite Solar Cells with Efficiencies Exceeding 22%. *Sol. RRL* **2022**, *6* (6), 2200053.
(11) Jošt, M.; Köhnen, E.; Al-Ashouri, A.; Bertram, T.; Tomšič, Š.; Magomedov, A.; Kasparavicius, E.; Kodalle, T.; Lipovšek, B.; Getautis, V.; Schlatmann, R.; Kaufmann, C. A.; Albrecht, S.; Topič, M. Perovskite/CIGS Tandem Solar Cells: From Certified 24.2% toward 30% and Beyond. *ACS Energy Lett.* **2022**, *7* (4), 1298−1307.
(12) Lin, R.; Xu, J.; Wei, M.; Wang, Y.; Qin, Z.; Liu, Z.; Wu, J.; Xiao, K.; Chen, B.; Park, S. M.; Chen, G.; Atapattu, H. R.; Graham, K. R.; Xu, J.; Zhu, J.; Li, L.; Zhang, C.; Sargent, E. H.; Tan, H. All-perovskite tandem solar cells with improved grain surface passivation. *Nature* **2022**, *603* (7899), 73−78.
(13) LONGi, LONGi sets a new world record of 33.9% for the efficiency of crystalline silicon-perovskite tandem solar cells, 2023. https://www.longi.com/en/news/new-world-record-for-the-efficiency-of-crystalline-silicon-perovskite-tandem-solar-cells/.
(14) Raifuku, I.; Ishikawa, Y.; Ito, S.; Uraoka, Y. Characteristics of Perovskite Solar Cells under Low-Illuminance Conditions. *J. Phys. Chem. C* **2016**, *120* (34), 18986−18990.
(15) Du, M.-H. Density Functional Calculations of Native Defects in $CH_3NH_3PbI_3$: Effects of Spin-Orbit Coupling and Self-Interaction Error. *J. Phys. Chem. Lett.* **2015**, *6* (8), 1461−1466.
(16) Kim, G.-W.; Petrozza, A. Defect Tolerance and Intolerance in Metal-Halide Perovskites. *Adv. Energy Mater.* **2020**, *10* (37), 2001959.
(17) Dong, Q.; Chen, M.; Liu, Y.; Eickemeyer, F. T.; Zhao, W.; Dai, Z.; Yin, Y.; Jiang, C.; Feng, J.; Jin, S.; Liu, S.; Zakeeruddin, S. M.; Grätzel, M.; Padture, N. P.; Shi, Y. Flexible perovskite solar cells with simultaneously improved efficiency, operational stability, and mechanical reliability. *Joule* **2021**, *5* (6), 1587−1601.
(18) Sutherland, L. J.; Vak, D.; Gao, M.; Peiris, T. A. N.; Jasieniak, J.; Simon, G. P.; Weerasinghe, H. Vacuum-Free and Solvent-Free Deposition of Electrodes for Roll-to-Roll Fabricated Perovskite Solar Cells. *Adv. Energy Mater.* **2022**, *12* (40), 2202142.
(19) Raifuku, I.; Ishikawa, Y.; Chiang, Y.-H.; Lin, P.-Y.; Li, M.-H.; Uraoka, Y.; Chen, P. Segregation-free bromine-doped perovskite solar cells for IoT applications. *RSC Adv.* **2019**, *9* (56), 32833−32838.
(20) Cheng, R.; Chung, C.-C.; Zhang, H.; Liu, F.; Wang, W.-T.; Zhou, Z.; Wang, S.; Djurišić, A. B.; Feng, S.-P. Tailoring Triple-Anion Perovskite Material for Indoor Light Harvesting with Restrained Halide Segregation and Record High Efficiency Beyond 36%. *Adv. Energy Mater.* **2019**, *9* (38), 1901980.
(21) Li, Z.; Zhang, J.; Wu, S.; Deng, X.; Li, F.; Liu, D.; Lee, C. C.; Lin, F.; Lei, D.; Chueh, C.-C.; Zhu, Z.; Jen, A. K. Y. Minimized surface deficiency on wide-bandgap perovskite for efficient indoor photovoltaics. *Nano Energy* **2020**, *78*, 105377.
(22) He, X.; Chen, J.; Ren, X.; Zhang, L.; Liu, Y.; Feng, J.; Fang, J.; Zhao, K.; Liu, S. 40.1% Record Low-Light Solar-Cell Efficiency by Holistic Trap-Passivation using Micrometer-Thick Perovskite Film. *Adv. Mater.* **2021**, *33* (27), 2100770.
(23) Freunek, M.; Freunek, M.; Reindl, L. M. Maximum efficiencies of indoor photovoltaic devices. *IEEE J. Photovolt.* **2013**, *3* (1), 59−64.
(24) Jiang, Q.; Zhang, X.; You, J. SnO_2: A Wonderful Electron Transport Layer for Perovskite Solar Cells. *Small* **2018**, *14* (31), 1801154.
(25) Kılıç, C.; Zunger, A. Origins of Coexistence of Conductivity and Transparency in SnO_2. *Phys. Rev. Lett.* **2002**, *88* (9), 095501.
(26) Mattioli, G.; Alippi, P.; Filippone, F.; Caminiti, R.; Amore Bonapasta, A. Deep versus Shallow Behavior of Intrinsic Defects in Rutile and Anatase TiO_2 Polymorphs. *J. Phys. Chem. C* **2010**, *114* (49), 21694−21704.
(27) Cojocaru, L.; Uchida, S.; Jayaweera, P. V. V.; Kaneko, S.; Nakazaki, J.; Kubo, T.; Segawa, H. Origin of the Hysteresis in I-V Curves for Planar Structure Perovskite Solar Cells Rationalized with a Surface Boundary-induced Capacitance Model. *Chem. Lett.* **2015**, *44* (12), 1750−1752.
(28) Tress, W.; Correa Baena, J. P.; Saliba, M.; Abate, A.; Graetzel, M. Inverted Current-Voltage Hysteresis in Mixed Perovskite Solar Cells: Polarization, Energy Barriers, and Defect Recombination. *Adv. Energy Mater.* **2016**, *6* (19), 1600396.
(29) Ebadi, F.; Taghavinia, N.; Mohammadpour, R.; Hagfeldt, A.; Tress, W. Origin of apparent light-enhanced and negative capacitance in perovskite solar cells. *Nat. Commun.* **2019**, *10* (1), 1574.
(30) Habisreutinger, S. N.; Noel, N. K.; Snaith, H. J. Hysteresis Index: A Figure without Merit for Quantifying Hysteresis in Perovskite Solar Cells. *ACS Energy Lett.* **2018**, *3* (10), 2472−2476.
(31) Alvarez, A. O.; Arcas, R.; Aranda, C. A.; Bethencourt, L.; Mas-Marzá, E.; Saliba, M.; Fabregat-Santiago, F. Negative Capacitance and Inverted Hysteresis: Matching Features in Perovskite Solar Cells. *J. Phys. Chem. Lett.* **2020**, *11* (19), 8417−8423.
(32) Ghahremanirad, E.; Almora, O.; Suresh, S.; Drew, A. A.; Chowdhury, T. H.; Uhl, A. R. Beyond Protocols: Understanding the Electrical Behavior of Perovskite Solar Cells by Impedance Spectroscopy. *Adv. Energy Mater.* **2023**, *13* (30), 2204370.
(33) Hu, Y.; Yang, Z.; Cui, X.; Zeng, P.; Li, F.; Liu, X.; Feng, G.; Liu, M. Construction of Charge Transport Channels at the NiO_x/Perovskite Interface through Moderate Dipoles toward Highly Efficient Inverted Solar Cells. *ACS Appl. Mater. Interfaces* **2022**, *14* (11), 13431−13439.
(34) Fathzadeh, A.; Abdollahi Nejand, B.; Moravvej-Farshi, M. K. Cation engineering for wide bandgap $CH_3NH_3Pb\ (I_{1-x}Br_x)_3$ perovskite solar cells. *OSA Continuum* **2021**, *4* (1), 1−14.
(35) Park, M.; Kim, J.-Y.; Son, H. J.; Lee, C.-H.; Jang, S. S.; Ko, M. J. Low-temperature solution-processed Li-doped SnO_2 as an effective electron transporting layer for high-performance flexible and wearable perovskite solar cells. *Nano Energy* **2016**, *26*, 208−215.
(36) Shen, Z.; Luo, X.; Shen, Y.; Liu, X.; Segawa, H.; Han, Q.; Han, L. Seed-Assisted Growth of Tin Oxide Transport Layer for Efficient Perovskite Solar Cells. *Sol. RRL* **2023**, *7* (12), 2300101.
(37) Wang, S.; Zhu, Y.; Liu, B.; Wang, C.; Ma, R. Introduction of carbon nanodots into SnO_2 electron transport layer for efficient and UV stable planar perovskite solar cells. *J. Mater. Chem. A* **2019**, *7* (10), 5353−5362.
(38) Kim, K. M.; Choi, B. J.; Lee, M. H.; Kim, G. H.; Song, S. J.; Seok, J. Y.; Yoon, J. H.; Han, S.; Hwang, C. S. A detailed understanding of the electronic bipolar resistance switching behavior in Pt/TiO_2/Pt structure. *Nanotechnology* **2011**, *22* (25), 254010.
(39) Kim, J.; Kim, K. S.; Myung, C. W. Efficient electron extraction of SnO_2 electron transport layer for lead halide perovskite solar cell. *npj Comput. Mater.* **2020**, *6* (1), 100.
(40) Srivastava, J.; Nahas, S.; Bhowmick, S.; Gaur, A. Electronic structure and transport in amorphous metal oxide and amorphous metal oxynitride semiconductors. *J. Appl. Phys.* **2019**, *126* (12), 125702.
(41) Matsuda, T.; Umeda, K.; Kato, Y.; Nishimoto, D.; Furuta, M.; Kimura, M. Rare-metal-free high-performance Ga-Sn-O thin film transistor. *Sci. Rep.* **2017**, *7* (1), 44326.
(42) Dou, M.; Persson, C. Comparative study of rutile and anatase SnO_2 and TiO_2: Band-edge structures, dielectric functions, and polaron effects. *J. Appl. Phys.* **2013**, *113* (8), 083703.

https://doi.org/10.1021/acsomega.4c03643
ACS Omega 2024, 9, 32893−32900